




The Urban Underground Space beneath the Karst Basin of Guilin, China, Revealed by Ambient Seismic Noise Tomography

Guiping Yu¹, Zhi Zhang^{*1,2}, Tao Xu³, Xuelai Li¹, Minling Wang¹, Xi Guo¹, Jiao Xu¹, Jue Hou^{4,5}, Guihong Guo⁶, and José Badal⁷

Abstract

Detection of hidden faults and sedimentary layers in the urban subsoil is significant for the utilization of the underground space, earthquake hazard mitigation, and so forth. Guilin, located in southwest China, is well known for the development of the most typical karst landform in the world and has become an international tourist city that needs scientific planning and knowledge of the urban underground space. After collecting waveform data recorded continuously over a period of about 1.5 months by a dense array of 114 short-period seismic stations installed in and around Guilin, we adopt ambient seismic noise cross-correlation method to extract Rayleigh-wave phase velocity dispersion curves within the period range from 0.5 to 5 s and to obtain a high-resolution S -wave velocity (V_S) model of the shallow crust above 9 km using surface-wave tomography. The vertical V_S gradient image indicates that the sediment thickness of the Guilin Karst basin is about 1–3 km. Sedimentary layers are relatively thick between Yanshan Mountain and Haiyang Mountain, and along the Yi river valley, where karst groundwater may be abundant and used as an important option for urban water supply. Both the absolute V_S velocity image and the relative V_S anomaly image clearly reveal the occurrence, location, and deep extension characteristics of major faults. Longsheng–Yongfu, Nanning–Guilin, Yaoshan–Yanshan, Baishi, and Guanyang–Hengyang may be regional deep faults cutting through the upper crust at least. The evolution of the basin is mainly controlled by the steep dipping Longsheng–Yongfu and Baishi faults, and partially controlled by the gently dipping Nanning–Guilin fault in the interior of the basin. The Nanning–Guilin fault is an active and partially buried fault obliquely crossing Guilin city. Urban seismic imaging, such as the new V_S tomography presented here, can play an important role in understanding tectonic and tectonic-subsidence earthquake hazards associated with these buried faults.



Cite this article as Yu, G., Z. Zhang, T. Xu, X. Li, M. Wang, X. Guo, J. Xu, J. Hou, G. Guo, and J. Badal (2022). The Urban Underground Space beneath the Karst Basin of Guilin, China, Revealed by Ambient Seismic Noise Tomography, *Seismol. Res. Lett.* **94**, 172–188, doi: [10.1785/0220220057](https://doi.org/10.1785/0220220057).

Supplemental Material

Introduction

Nowadays, the investigation of the underground space has become an important target for subsequent urban planning and construction, and its use evolves toward integration, deepening, and ecologicalization, which poses greater demands on the exploration of the urban subsoil (Zhao *et al.*, 2017; Wang *et al.*, 2019). The goal is to accurately detect the distribution of hidden faults, sedimentary layers (strata above crystalline basement, including loose sediment, weathered layer, and consolidated sedimentary rock), karst structure, groundwater, and so forth. In particular, the detection of hidden faults in cities and their surroundings has an important impact on sustainable urban development, which involves earthquake disaster prevention, infrastructure construction, urban planning, and so forth (Li, 2011; Adly *et al.*, 2017; Diaz *et al.*, 2017, 2020;

Zhao *et al.*, 2017; Vassallo *et al.*, 2019). Therefore, it is important to carry out a comprehensive exploration of the urban underground space and reveal the detailed features of geological structures such as hidden faults. However, due to the population density and concentration of buildings, strong

1. Guilin University of Technology, Guilin, China,  <https://orcid.org/0000-0003-3424-2174> (GY);  <https://orcid.org/0000-0002-1025-8107> (MW); 2. Guangxi Key Laboratory of Exploration for Hidden Metallic Ore Deposits, Guilin, China; 3. State Key Laboratory of Lithosphere Evolution, Institute of Geology and Geophysics, Chinese Academy of Sciences, Beijing, China; 4. University of Chinese Academy of Sciences, Beijing, China; 5. Institute of Geophysics, China Earthquake Administration, Beijing, China; 6. The Key Laboratory of Mechanics on Disaster and Environmental in Western China, Lanzhou University, Lanzhou, China,  <https://orcid.org/0000-0002-1986-6723> (GG); 7. Physics of the Earth Sciences B, University of Zaragoza, Zaragoza, Spain

*Corresponding author: zhangzhi@glut.edu.cn

© Seismological Society of America

electromagnetic interference, and nondestructive limits, common electromagnetic methods (such as magnetotelluric, controllable source audio magnetotelluric, transient electromagnetic, etc.), and active seismic exploration methods are difficult to carry out effectively (Yi *et al.*, 2008; Li *et al.*, 2010; Li, 2011; Zhang, Xu, and Li, 2019).

Ambient seismic noise tomography is one of the most important advances in the field of seismology since the beginning of the twenty-first century. It plays an increasingly important role in the use of vibrational signals from random field sources to obtain high-resolution images of subsurface structure (Shapiro *et al.*, 2005; Weaver, 2005; Yao *et al.*, 2006; Bensen *et al.*, 2007; Yang *et al.*, 2007). In this method, the empirical Green's function (EGF) is obtained by calculating the cross correlation of long-time ambient seismic noise records between station pairs, then extracting the surface-wave dispersion curve and inverting for shear wave velocity structure of the underground space (Shapiro and Campillo, 2004). Ambient seismic noise tomography method eliminates the dependence on the seismic source and has the advantages of large detection depth (the maximum detection depth can reach the top of the upper mantle), low acquisition cost, strong anti-interference ability, and environmental friendliness compared with traditional active source methods (Nolet, 2008; Zhang, Liu, *et al.*, 2019). In addition, it can make full use of short-period surface-wave signals in ambient noise, overcoming the serious attenuation of high-frequency components in traditional seismic surface waves, and is more suitable for application in densely populated urban areas. In recent years, there have been many successful cases of this widely used method in the field of shallow crustal structure imaging (Picozzi *et al.*, 2009; Goertz *et al.*, 2012; Badal *et al.*, 2013; Cheng *et al.*, 2015; Li *et al.*, 2016, 2020; Diaz, *et al.*, 2017, 2020; Liu *et al.*, 2018; Fang *et al.*, 2019; Liang *et al.*, 2019; Vassallo *et al.*, 2019; Yu *et al.*, 2020; Zeng *et al.*, 2020; Chen *et al.*, 2021; Zheng, Bai, *et al.*, 2021; Zheng, Fan, *et al.*, 2021).

Guilin, located in the southwest of China, is famous for its development of the most typical and ornamental karst landforms in the world. It is known as the “capital of karst” by the international karst academic community. Therefore, Guilin has become an international tourist city in China since 2012. In 2018, Guilin became one of the first three cities in the innovation demonstration zone of the country's sustainable development agenda, so the urban construction of Guilin and its jurisdictions has entered a new stage (Chen and Tang, 2018). However, the widespread geological problems such as hidden faults and karst structures restrict the further development and utilization of the underground space. Guilin's karst landform is environmentally vulnerable, and this is reflected in two aspects: water resources and geology. The former is embodied in the loss of surface water. Although the annual average rainfall in Guilin is abundant, the widespread exposure of limestone makes it difficult to preserve surface water for a long time, and water shortage will still be faced in spring and

autumn. Groundwater is generally abundant in karst development areas where carbonate sediments are usually thick (Liu *et al.*, 2015). Therefore, it is of great significance for urban construction to connect the study of sediment, karst structure, and groundwater. The latter is embodied in geological disasters, including collapse, subsidence, tectonic-subsidence earthquakes, and so forth. Among them, the tectonic-subsidence earthquake, which is closely related to both fault structure (such as the active Nanning–Guilin fault) and karst subsidence, is the most harmful (Miu, 1998; Yu and Gao, 2017; Chen and Tang, 2018). To solve the earlier problems, it is necessary to obtain high-resolution images of the urban underground structure. In addition, the previous studies on the underground structure of Guilin are mainly based on data from shallow geological surveys, local electromagnetic explorations, and historical earthquake records (Miu, 1998; Feng *et al.*, 2001; Wan *et al.*, 2001; Zhang *et al.*, 2007; Nie *et al.*, 2019; Jiang *et al.*, 2020; Li *et al.*, 2020), which lack the support of deep geophysical exploration.

Based on the earlier reasons, in 2020 we deployed a dense short-period seismic array generally covering Guilin city, and further carried out ambient seismic noise tomography based on Rayleigh-wave phase velocity dispersion, to find out the deep morphology of the main faults and the distribution pattern of sedimentary layers in Guilin. Here, we analyze the risks of tectonic and tectonic-subsidence earthquakes and karst collapse, providing deep geophysical support for earthquake prevention and disaster mitigation, as well as for the improvement of urban intensification and sustainable development.

Geological Setting

Guilin area is located to the west of the Nanling latitudinal tectonic belt and to the northeast of the Guangxi Autonomous Region (Chen and Tang, 2018). It is a north–south-trending karst basin with typical karst peak forests (characterized by isolated hills rising from an alluvium plain) and karst peak clusters (clustered limestone peaks that share a common base with deep depressions) (Liang and Xu, 2014). Famous karst scenic spots are mainly concentrated in the urban district of Guilin, Yangshuo County, and along the Li River. The most widely distributed bedrock in this area is Devonian, which is mainly composed of pure and thick carbonate rocks (Fig. 1a). The Quaternary soil layer cover in the plain area is about 0–30 m thick, mainly composed of subsand–soil, subclay, clay, and boulder clay. Detailed lithology distribution and stratigraphic column information can be seen in relevant references (Bureau of Geology and Mineral Resources of Guangxi Province [BGMGRGX], 1985; Yuan, 1997; Tang and Day, 2000; Feng *et al.*, 2001; Huang *et al.*, 2013; Zhou *et al.*, 2015). The trend of karst groundwater channels is mainly controlled by a series of north–south folds and faults (Liu *et al.*, 2015).

Guilin basin is a faulted basin with many narrow ladder-like fault blocks. The fault block movement in the basin decomposed the Late Cretaceous–Early Tertiary peneplain into mountains

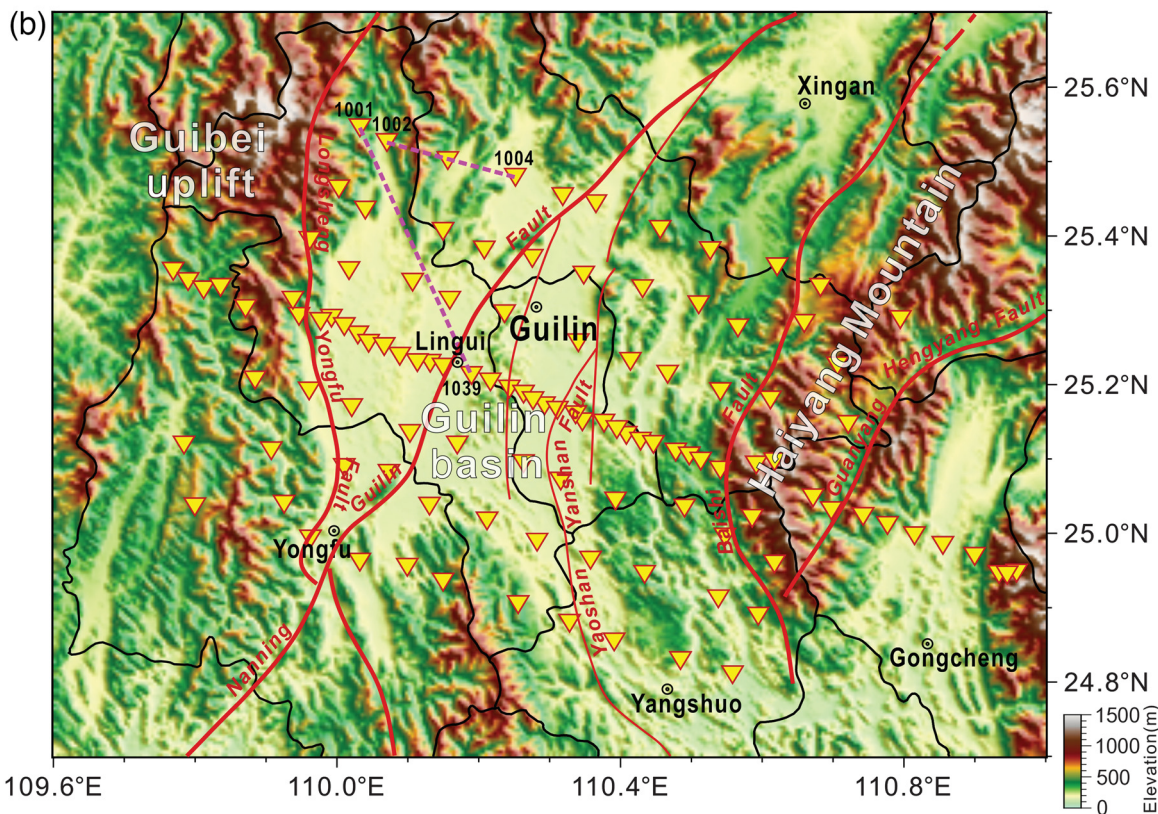
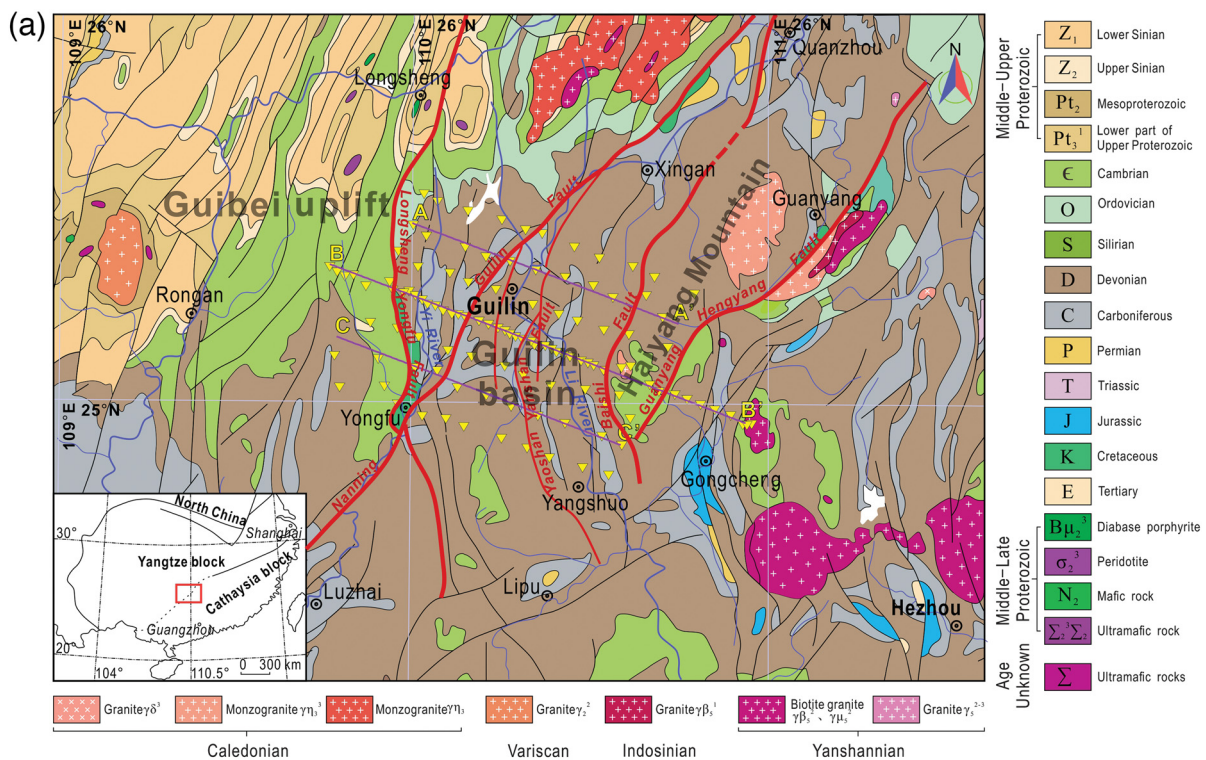


Figure 1. (a) Geological map of the study area. The red rectangle inside the box in the lower left corner outlines the area of interest. Yellow inverted triangles indicate short-period seismic stations. Thick red lines and thin black lines represent major faults and secondary faults, respectively. Purple lines indicate three profiles AA', BB', and CC' that cross the Guilin basin from

northwest to southeast (we will refer to these profiles later). (b) Topographic map of the study area. Yellow inverted triangles and red thick lines have the same meaning as panel (a). Purple dotted lines represent the ray paths between station pairs 1001–1039 and 1002–1004 (we will use them as examples to show the extraction process of dispersion curves later).

and valleys with different heights (Chen and Liu, 1980). Under the control of the basin's nearly north-south trend, most of the faults on the east and west edges are nearly north-south. In the northeast of the basin, affected by the Xing'an graben, the faults have a north-northeast trend and extend to the middle of the basin (Fig. 1). The north and south edges are mainly controlled by northeast and northwest-trending faults.

As early as the Cretaceous, the Guilin basin had taken shape. At the end of the Cretaceous, the landform of the Guilin area was in a peneplain state. Then, the Himalayan movement brought the Guilin basin to a new stage of development. In the Tertiary period, the peneplain was destroyed, and the mountains around the basin gradually rose. The new fault block movement differentiated the basin into mountains and valleys. Each geomorphic unit is bounded and further divided into several blocks by faults. The humid and warm climate conditions of the Tertiary created the peak forest landform, such that the height of each peak forest mountain decreases from east to west (Chen and Liu, 1980; BGMRGX, 1985).

Main faults in the Guilin area include the Longsheng-Yongfu fault, Nanning-Guilin fault, Yaoshan-Yanshan fault, Baishi fault, and Guanyang-Hengyang fault (Bureau of Geology of Guangxi Province [BGGX], 1976; BGMRGX, 1985; Ma *et al.*, 2004). Among them, the Longsheng-Yongfu fault runs through the whole study area from north to south (Fig. 1). It is a thrust fault with dipping direction northwest-west and a dip angle of 45°–85°. This fault experienced Caledonian, Hercynian, Indosinian, and Yanshanian tectonic activities and is characterized by complex morphology, multilevel deformation, and multistage tectonic activity (Wei and Zhou, 2000; Zhang *et al.*, 2001).

The Nanning-Guilin fault starts from Quanzhou County in the northeast, passes through Xing'an, Guilin, Nanning, and Chongzuo in the southwest, and then gets in Vietnam, passing obliquely through Guangxi with a strike of 40°–50° northeast (BGMRGX, 1985; Ma *et al.*, 2004). Its northern section is also called Guilin-Laibin fault or Lingchuan-Yongfu fault and is composed of several roughly parallel subfaults. The fault zone has a width of several kilometers, cuts from the Cambrian to the Cretaceous, and dips both southeast and northwest, with a dip angle of 30°–60°. The Nanning-Guilin fault is an inherited fault with long-term activity. It is still active since the Cenozoic.

The Yaoshan-Yanshan fault runs along the west side of the Yaoshan anticline. Its strike changes from north-northeast in the north to north-northwest in the south, with an east-dipping direction and a dip angle of 30°–60° (BGGX, 1976; BGMRGX, 1985).

The Baishi fault starts from Quanzhou County in the north, passes through Longmu and Anhe to Baishi in Xing'an County and Dajing in Yangshuo County in the south, then turns to south-southeast, and reaches near Shazi in Pingle County, with a total length of 180 km. This fault and its adjacent folds are arc-shaped standing out to the west, with an overall north-

south strike, a west-dipping direction, and a dip angle of 37°–82° (BGMRGX, 1985; Lu *et al.*, 2019).

Data and Method

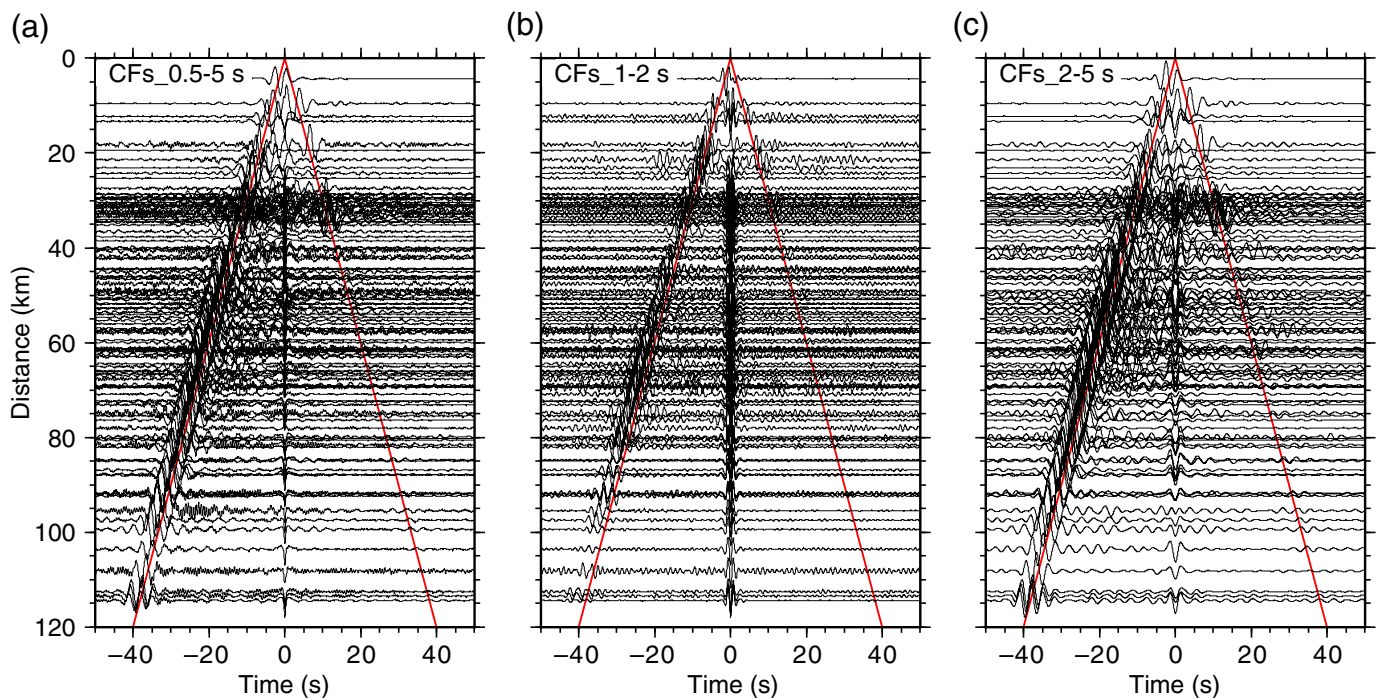
Seismic noise data

From August to September 2020, we deployed a 2D dense short-period seismic array in the study area (109.66°–111.06° E, 24.69°–25.65° N), as shown in Figure 1. The array consisted of seven northwest-southeast-trending survey lines with a line spacing of ~10 km and an inline station spacing of ~7 km. The array was composed by a total of 114 stations, which were used in three observation periods of ~15 days over 1.5 months. During the first two periods, ambient noise was recorded by the rectangular array continuously. Throughout the third period of time, half of the stations of the rectangular array were moved to carry out the extension and densification of the middle survey line. Thus the middle survey line (profile BB' in Fig. 1a) became a 130 km long antenna with numerous stations separated by ~2 km. For field operations, we used three-component short-period seismographs (QS-10B) with integrated digital acquisition system and geophone with a frequency band of 0.1–250 Hz (2 Hz corner frequency). The raw data sampling rate was 100 Hz.

Data preprocessing

Both theory and practice demonstrate that the EGF between station pairs can be obtained by deriving the cross-correlation function (CCF) of ambient seismic noise superimposed for a long time (Sabra *et al.*, 2005; Campillo and Roux, 2015). In this article, we use the cross correlation of the vertical-component signal to extract Rayleigh waveforms. Before carrying out cross correlation, data preprocessing must first be performed at each station, including cutting the data to a duration of 1 hr, resampling from 100 to 20 Hz, removing instrument response, detrending the zero-line slope and mean, band-pass filtering (0.2–10 s), normalization in the time domain, and spectral whitening by running absolute mean normalization (Bensen *et al.*, 2007; Badal *et al.*, 2013). After data preprocessing, we compute the CCFs of vertical components between any station pair for each hour. The CCFs for each station pair and different hours are normalized and linearly stacked to obtain the final CCFs. It should be noted that if stations were moved around and only recorded for 15 days at each location then only the 15-day groupings can be correlated with each other. Figure 2 displays the CCFs of the signal recorded at station 1001 in the northernmost part of the array with the noise signals recorded at the other adjacent stations for three period bands of 0.5–5, 1–2, and 2–5 s. Clear Rayleigh waveforms can be seen on all graphs.

In the case of a uniform distribution of noise sources, the amplitudes of the CCFs on the positive and negative semiaxes should be symmetrical. However, the amplitudes on the negative semiaxes are stronger than on the positive semiaxes (Fig. 2), indicating an uneven distribution of noise sources



in the Guilin area. To remove the influence of the uneven distribution of noise sources, symmetrical amplitudes are obtained by stacking the positive and negative branches of the CCFs to calculate surface-wave dispersion curves (Yang *et al.*, 2007), as explained in the next section.

Extraction of dispersion curves

Based on the time-domain harmonic far-field approximation of the fundamental mode surface-wave Green's function, we use the image transformation technique (Yao *et al.*, 2006) to extract Rayleigh-wave phase-velocity dispersion curves from EGFs (Fig. 3a,b). Considering the signal-to-noise ratio (SNR) of the field data, we extract the dispersion curves within a period range of 0.5–5 s, using a sampling interval of 0.1 s. In this study, the SNR, which is period or frequency dependent, is defined as: $\text{SNR}(f) = (\text{Maximum amplitude of envelope around frequency } f \text{ in the signal window}) / (\text{Mean amplitude of envelope of 150 s long noise window right after the signal window})$. Taking the uppermost illustration in Figure 3a as an example, the bottom blue part of the trace shows the signal (within phase velocity window) and the red part shows the noise (right after the signal window). We only select those EGFs with separations greater than twice the wavelength and with SNR above 5 (Luo *et al.*, 2015). At the same time, we exhaustively consider the continuity of the dispersion curves and their similarity for adjacent station pairs. Furthermore, to accurately identify short-period dispersion curves that vary greatly in different landforms, we also take into account the characteristics of dispersion data relative to other areas (Picozzi *et al.*, 2009; Cheng *et al.*, 2015; Liang *et al.*, 2019; Vassallo *et al.*, 2019; Li *et al.*, 2020; Yu *et al.*, 2020; Zeng *et al.*, 2020; Chen *et al.*, 2021; Zheng, Bai, *et al.*, 2021; Zheng, Fan,

Figure 2. Stacks of cross-correlation functions (CCFs) of the vertical-component signal recorded at the northernmost station 1001 with the noise signals recorded at the other adjacent stations, plotted against distances between stations. The graphs here included correspond to different period ranges: (a) 0.5–5, (b) 1–2, and (c) 2–5 s. Rayleigh waveforms can be seen on all graphs. Red straight lines are the time–distance curve for a trial seismic velocity of 3 km/s. The color version of this figure is available only in the electronic edition.

et al., 2021), in addition to restrict the absolute phase velocity value to the range of 2.4–3.5 km/s.

After selection, we finally obtain 4148 high-quality fundamental Rayleigh-wave phase velocity dispersion curves, with average velocity values varying slowly from 2.76 km/s for 0.5 s to 3.17 km/s for 5 s (Fig. 3c). The phase velocity is generally high, which is consistent with the surface geological characteristics of thin loose sediments and widely exposed bedrock in the Guilin area. Figure 3d shows the number of ray paths for each period using a histogram of vertical bars: the largest number 3408 corresponds to 2.1 s, whereas the smallest 709 corresponds to 0.5 s.

Phase velocity map inversion

The dispersion curve measured from the CCF is called interstation dispersion, which is the average response to the seismic velocity structure along the path. Therefore, we first use the generalized inversion method based on a continuous model space (Tarantola and Valette, 1982; Montagner and Nataf, 1986; Yao *et al.*, 2010) to obtain local dispersion curves at individual grid points, so as to prepare for the next S-wave velocity (V_s) inversion. The local azimuthally varying Rayleigh-wave

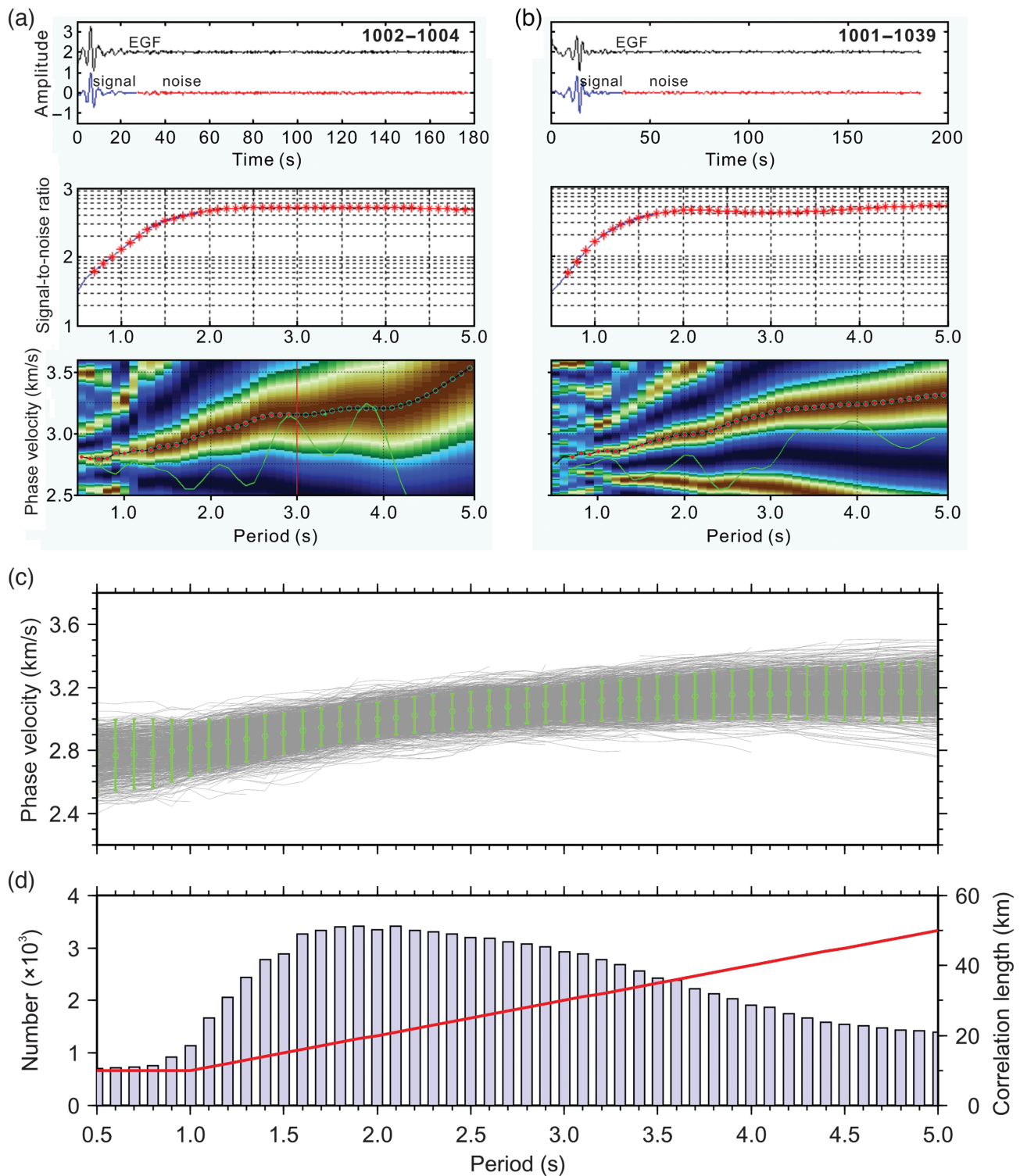


Figure 3. (a,b) Examples for extracting Rayleigh-wave phase velocity dispersion curves corresponding to station pairs 1002–1004 and 1001–1039. From top to bottom are the EGF after symmetrical superposition, signal-to-noise ratio, and phase velocity dispersion curve (The red dots indicate phase velocity values for each period; the green line denotes the theoretical group velocity dispersion curve calculated from the picked phase velocity dispersion; and the period less than the corresponding value of the red line meets the

requirement that the interstation distance is greater than twice the wavelength), respectively. (c) Phase velocity dispersion curves in the 0.5–5 s period range extracted from CCFs. The total number of dispersion curves (gray lines) is 4148. Green circles indicate mean values of phase velocity. The green error segments represent twice the standard deviation for each period. (d) Number of ray paths for each period (histogram of vertical bars). The red line indicates the isotropic velocity correlation length for inversion.

phase velocity $c(\omega, M, \psi)$ at location M for each angular frequency ω and azimuth ψ can be expressed as

$$c(\omega, M, \psi) = c_0(\omega)[1 + a_0(\omega, M) + a_1(\omega, M) \cos 2\psi + a_2(\omega, M) \sin 2\psi], \quad (1)$$

in which $c_0(\omega)$ is the reference phase velocity (usually the average of all observed phase velocities at a certain frequency), and a_0 and a_i (with $i = 1, 2$) are the isotropic phase velocity perturbation and the azimuthally anisotropic coefficients, respectively. The inversion for a_0 (or a_i) is controlled by three parameters: the standard error of phase velocity (or the azimuthally anisotropic coefficients) measurements σ_d , the priori parameter error σ_p (which constraints the anomaly amplitude), and the spatial correlation length L_c (which constraints the smoothness of the model parameters).

In this study, we do not consider the anisotropy, that is, in the inversion process, we set the standard error of anisotropic parameters to a value as small as possible (e.g., 0.0001) and set the anisotropic velocity correlation length to be as large as possible (e.g., more than 10 times of the isotropic velocity correlation length). Therefore, only the phase velocity changes after inversion, and the result is most affected by the isotropic velocity correlation length. Generally, the smaller the wavelength, the smaller the selected correlation length. In addition, the higher the SNR, the smaller the selected correlation length. Its minimum value is usually required to be greater than one-third times the wavelength. In this article, we comprehensively consider the wavelength corresponding to different periods, the SNR of the data, the results of checkerboard tests, and the scale of regional geological units to determine the correlation length for each period, which logically is an increasing function as the period increases (red line in Fig. 3d). We use a $0.04^\circ \times 0.04^\circ$ -sized grid to parameterize the inversion domain. In the inversion process, those dispersion data with residuals greater than twice the standard deviation are automatically discarded. Figure 4 shows surface-wave phase velocity patterns for different periods, in which the relatively low-velocity anomalies near the Longsheng–Yongfu and Nanning–Guilin faults are the most significant.

S-wave velocity models

After inverting phase velocity, we obtain many dispersion curves, each of which refers to a grid point. For a layered earth model, the Rayleigh-wave phase velocity for different periods is related to P -wave velocity (V_P), V_S , and density, in which V_S has the greatest influence (Schwab and Knopoff, 1972). Here, we follow the iterative damped least-squares inversion method developed by Herrmann and Ammon (2013) to invert the V_S structure using the Computer Programs in Seismology Version 3.30 (CPS330; Herrmann, 2013) software package. In the inversion process, the initial model was divided into 0.5 km thick layers. In a Poisson medium with a uniform half-space,

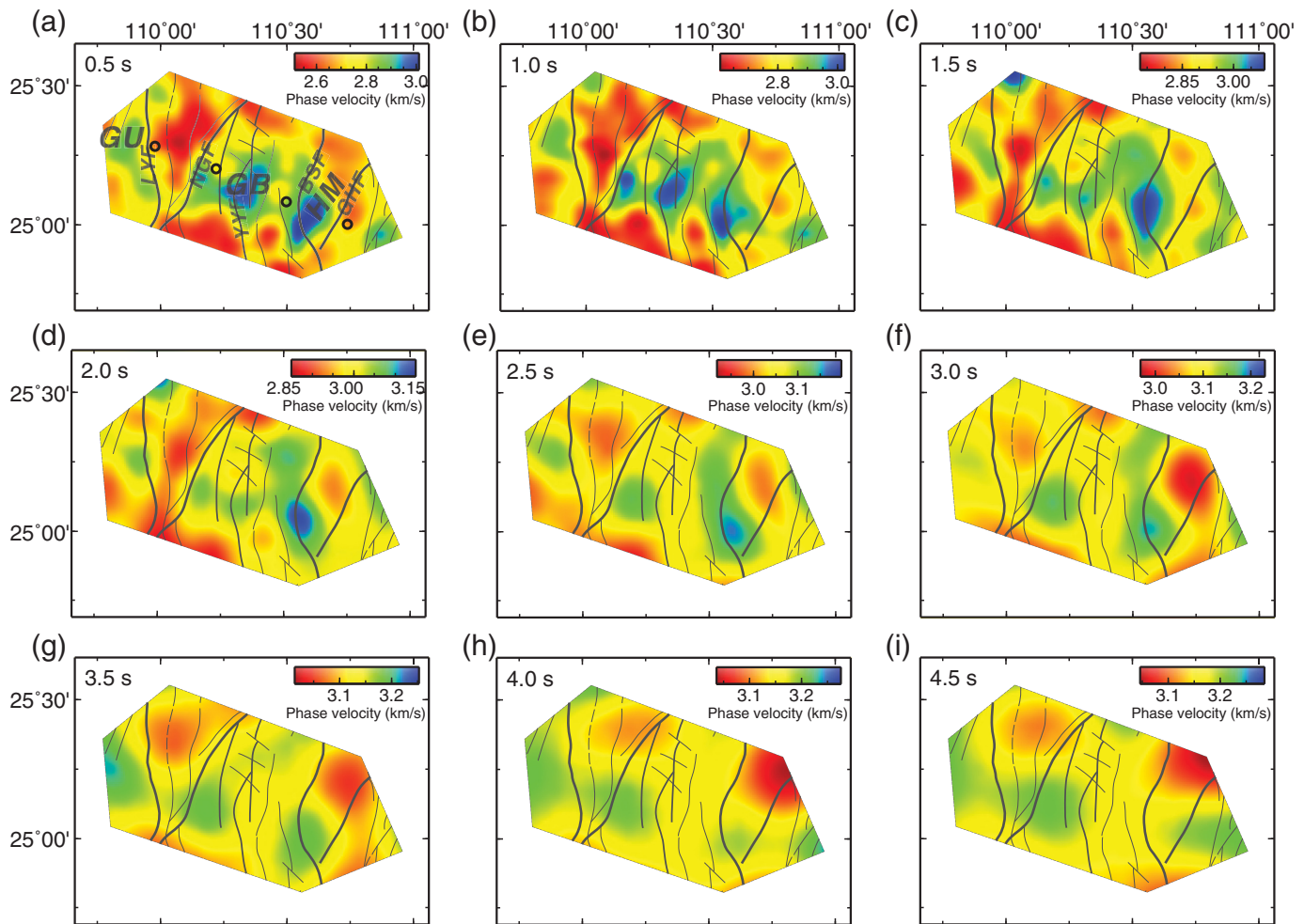
V_S at a depth of one-third wavelength of Rayleigh wave is about 1.1 times the phase velocity (Shearer, 2009; Fang *et al.*, 2015). Accordingly, we construct an initial velocity model (see gray dashed line in Fig. 5) based on the average dispersion curve for all station pairs and the previous empirical relationship. Nevertheless, it should be noted that the first 0–4.5 km of the initial model are estimated values based on the average dispersion curve and appropriate smoothing. A fixed value of 3.6 km/s is adopted below 8 km, leaving a smooth transition of the model in the depth interval 4.5–8 km. The V_P/V_S ratio is set to 1.70 and the initial density to 2.8 g/cm³. In the inversion process, the density is updated according to the Nafe–Drake relationship (Nafe and Drake, 1957). To ensure the inversion stability, we set the maximum depth of the initial model to 15 km. However, unless otherwise specified, we do not display beyond the first 0–9 km of the inversion model. Figure 5 shows the inversion results for V_S referred to four sample grid points. In this illustration, we show both the initial velocity model and the current model for each sample point. We also show the original phase velocity dispersion curve and the synthetic dispersion curve obtained by forward modeling from the current velocity–depth model. It should be noted that the initial velocity model has small influence on the final 1D V_S inversion result (see the Resolution test and impact of the initial model section for details), so the simple model based on an empirical estimation is used as initial velocity model in this article.

Results

Horizontal and vertical velocity sections

Based on the previous inversion results, we obtain a high-resolution V_S model of the shallow crust above 9 km in the Guilin area. Figure 6 shows horizontal V_S slices at different depths from 1 to 9 km. Slices above 3 km (Fig. 6a–c) indicate that relatively low- or high-velocity anomalies are alternately distributed, which corresponds well to basin-range tectonics on the surface, and clearly reveals the fault block structural pattern of the Guilin basin. At increasing depths (Fig. 6d–f), the influence of the shallow loose sedimentary layer gradually weakens, and low-velocity anomalies are distributed along Longsheng–Yongfu, Nanning–Guilin, Yaoshan–Yanshan, Baishi, Guanyang–Hengyang, and other large regional faults. Although the resolution of the V_S images gradually reduces at deeper depths due to the limitation of the wavelength used, the arc-shaped Baishi fault together with the Haiyang mountain remain highly significant (Fig. 6g–i).

To further reveal the occurrence and scale of major faults and the thickness of sedimentary layers, we draw phase velocity and V_S vertical sections along three profiles AA', BB', and CC' that cross the Guilin basin from northwest to southeast (purple lines in Fig. 1a). Furthermore, to highlight the lateral and vertical variation characteristics of the V_S structure, we also calculate the relative V_S anomaly and the vertical V_S gradient for the aforementioned profiles. The relative anomaly of V_S is the percentage of the velocity at each grid point relative to the



average velocity at the same depth. All these results (sections) can be seen in Figure 7 (transect BB') and in Figures S1 (transect AA') and S2 (transect CC') (available in the supplemental material to this article). Because the multiattribute images shown in these three sections have similar features, we will analyze the deep extension and spatial distribution characteristics of the main structures revealed by the longest profile BB' (Fig. 7).

Profile BB' (Fig. 7a) crosses three main tectonic units from west to east, including Guibei uplift, Guilin basin (or Guilin arc fold-fault belt), and Haiyang Mountain (or Haiyangshan fold-fault belt). The phase velocity image (Fig. 7b) and V_S image (Fig. 7c) intuitively show that the Longsheng–Yongfu, Nanning–Guilin, Yaoshan–Yanshan, Baishi, and Guanyang–Hengyang faults are boundaries of relatively high- and low-velocity anomalies at shallow depths (≤ 2 km). Low-velocity anomalies beneath the Longsheng–Yongfu and Baishi faults continue to extend to deeper depths (Fig. 7c), clearly separating the three major tectonic units mentioned. The combination of absolute and relative V_S velocity anomaly images (Fig. 7d) offers the possibility to roughly track the deep extension of the main faults by following the low-velocity anomaly or the boundary between the high- and low-velocity anomalies. The results show that Nanning–Guilin

Figure 4. (a–i) Surface-wave phase velocity patterns for different periods (upper left corner) and corresponding average phase velocities for each period are 2.76, 2.82, 2.91, 3.00, 3.06, 3.10, 3.13, 3.16, and 3.17 km/s. The circles in (a) indicate the positions of the four grid points in Figure 5. BSF, Baishi fault; GB, Guilin basin; GHF, Guanyang–Hengyang fault; GU, Guibei uplift; HM, Haiyang Mountain; LYF, Longsheng–Yongfu fault; NGF, Nanning–Guilin fault; and YYF, Yaoshan–Yanshan fault.

and Yaoshan–Yanshan faults tend to the southeast, whereas the Longsheng–Yongfu, Baishi, and Guanyang–Hengyang faults tend to the northwest, which is consistent with the observation on the surface.

To reveal the variation in sedimentary layer thickness, we need to track the high-velocity discontinuity between the sedimentary layer and the crystalline basement (Thybo *et al.*, 2003; Artemieva and Thybo, 2013). Because surface waves are less sensitive to velocity interfaces, we use the vertical V_S gradient to enhance the characteristics of this high-velocity discontinuity (Yu *et al.*, 2020). Figure 7e shows that the vertical V_S gradient is close to its maximum at about 1–3 km depth, indicating a rapid increase in velocity. This depth may be the high-velocity discontinuity between the sedimentary layer and the

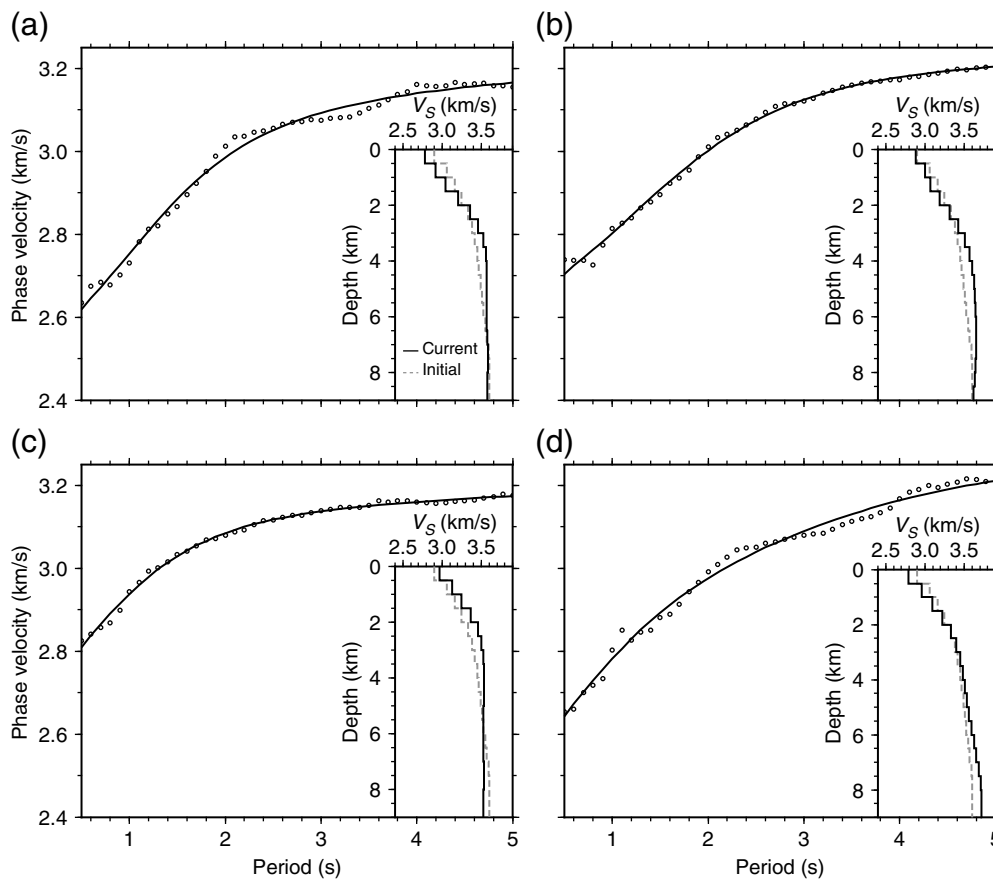


Figure 5. (a–d) Inversion results for S-wave velocity referred to four sample grid points: (109.98° E, 25.29° N), (110.22° E, 25.21° N), (110.50° E, 25.09° N), and (110.74° E, 25.01° N). Both the initial velocity model (gray dashed line) and the current model (black solid line) are shown in the lower right quadrant of each plot. For each sample point, the dotted curve is the original phase velocity dispersion curve, whereas the solid line is the synthetic dispersion curve obtained by forward modeling from the current velocity–depth model.

crystalline basement. However, possibly due to the influence of fault fracture zone, the maximum gradient is not completely continuous in the transverse direction, so we cannot track and obtain a continuous 2D or 3D sediment thickness distribution map. Considering that the depth of the maximum gradient roughly corresponds to the V_S isosurface of 3.4 km/s, we then use this isosurface (Fig. 8a) to approximate the sediment thickness distribution map. The results show that the sediment thickness in the Haiyang mountainous area is the thinnest, about 1–2 km, and the basement may be exposed on the surface locally. However, in the Guibei uplift, northwest Guilin city, and in the Yanshan area, the sediment thickness reaches about 3 km. The thickest sedimentary cover, which can reach a thickness of 3–4 km locally, is located between Yanshan Mountain and Haiyang Mountain (i.e., along the Li River), as well as in the Yi River Valley in Yongfu County and north. In addition, we found that the V_S isosurface of 3.0 km/s (Fig. 8b) corresponds well with the thickness of loose sediments or strongly weathered layers. Where there are mountains, the

depth of this isosurface tends to zero, whereas along the Longsheng–Yongfu and Nanning–Guilin faults, due to the thick loose sediments and strongly weathered layers, the depth of the isosurface can reach 1–2 km locally.

Furthermore, it is worth noting that although the maximum V_S gradient at about 1–3 km depth is not laterally continuous, the discontinuous positions or gaps correspond well with the main faults on the surface (Fig. 7e). Therefore, connecting the outcrop of the fault on the surface with the breakpoint of the high-velocity discontinuity can help track (at least partially) the deep extension of the fault. According to the V_S velocity sections along profiles AA' and CC' (Figs. S1 and S2, respectively), it shows that the basement below the Longsheng–Yongfu, Nanning–Guilin, Yaoshan–Yanshan, Baishi, and Guanyang–Hengyang faults is damaged or stepped in different degrees, indicating that they are at least large basement faults. The Nanning–Guilin fault extends

from northeast to southwest and intersects the Yaoshan–Yanshan fault in the north and the Longsheng–Yongfu fault near Yongfu County in the south.

Resolution test and impact of the initial model

To analyze the lateral resolution of the results provided by phase velocity inversion, we perform a checkerboard test as shown in Figure 9, taking periods of 1, 2, 3, and 4 s as reference. In the test, the inversion parameters such as effective ray-path coverage, average phase velocity, grid size, and isotropic correlation length are the same as in real data inversion. Figure 9a–d shows the effective ray-path coverage for each period. Figure 9e–h shows the period-dependent variable-size lattice geometry by applying alternating velocity increments of $\pm 5\%$. Logically, the grid size (velocity anomaly) of the checkerboard also gets larger, 0.12°, 0.16°, 0.20°, and 0.24°, as the period increases from 1 to 4 s, respectively. Increasing average phase velocities of 2.82, 3.00, 3.10, and 3.16 km/s are taken as reference. The checkerboard recovery results shown in

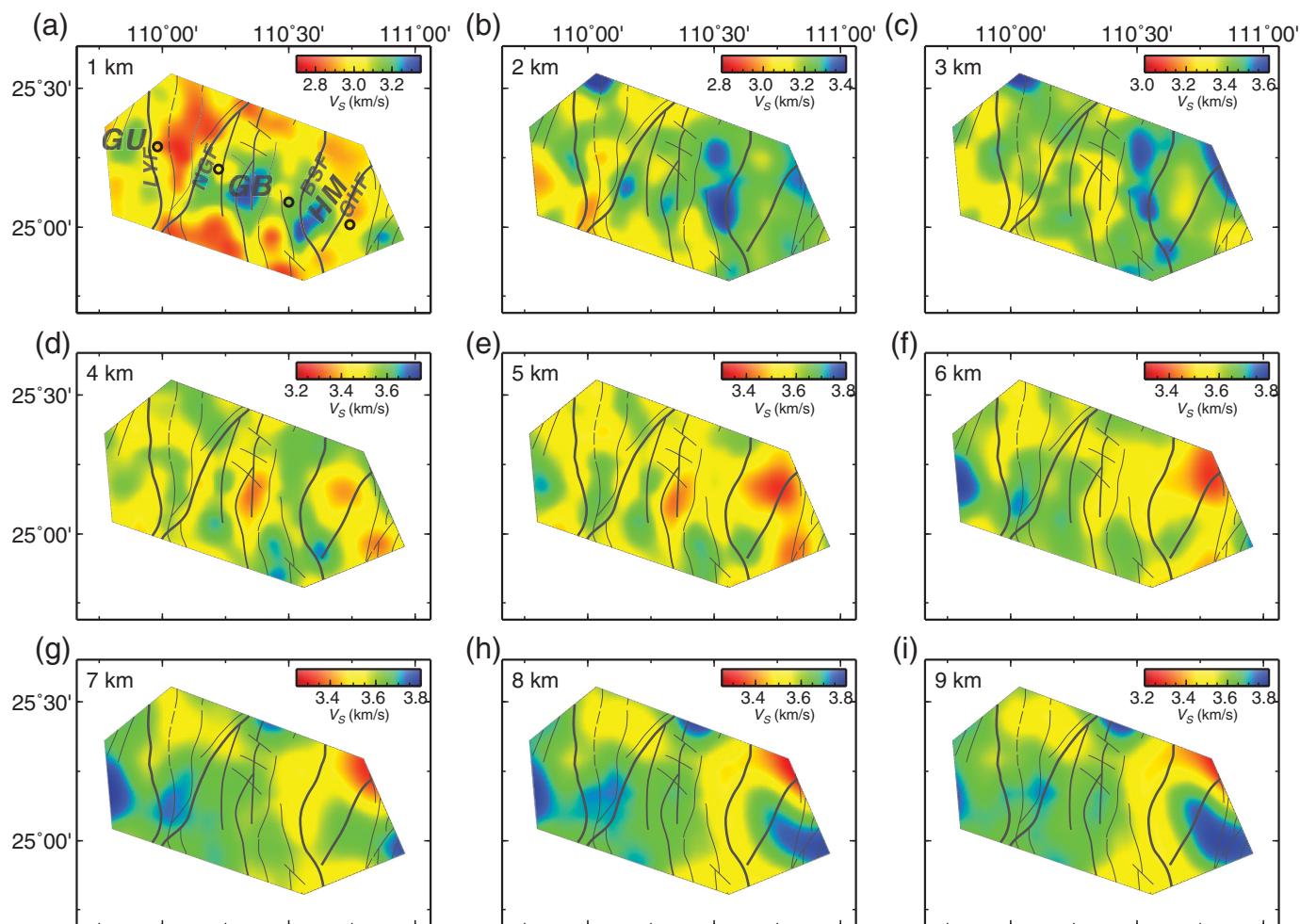


Figure 9i-l indicate that the phase velocity inversions have a good resolution for the selected periods and the supposed variable-size anomalies.

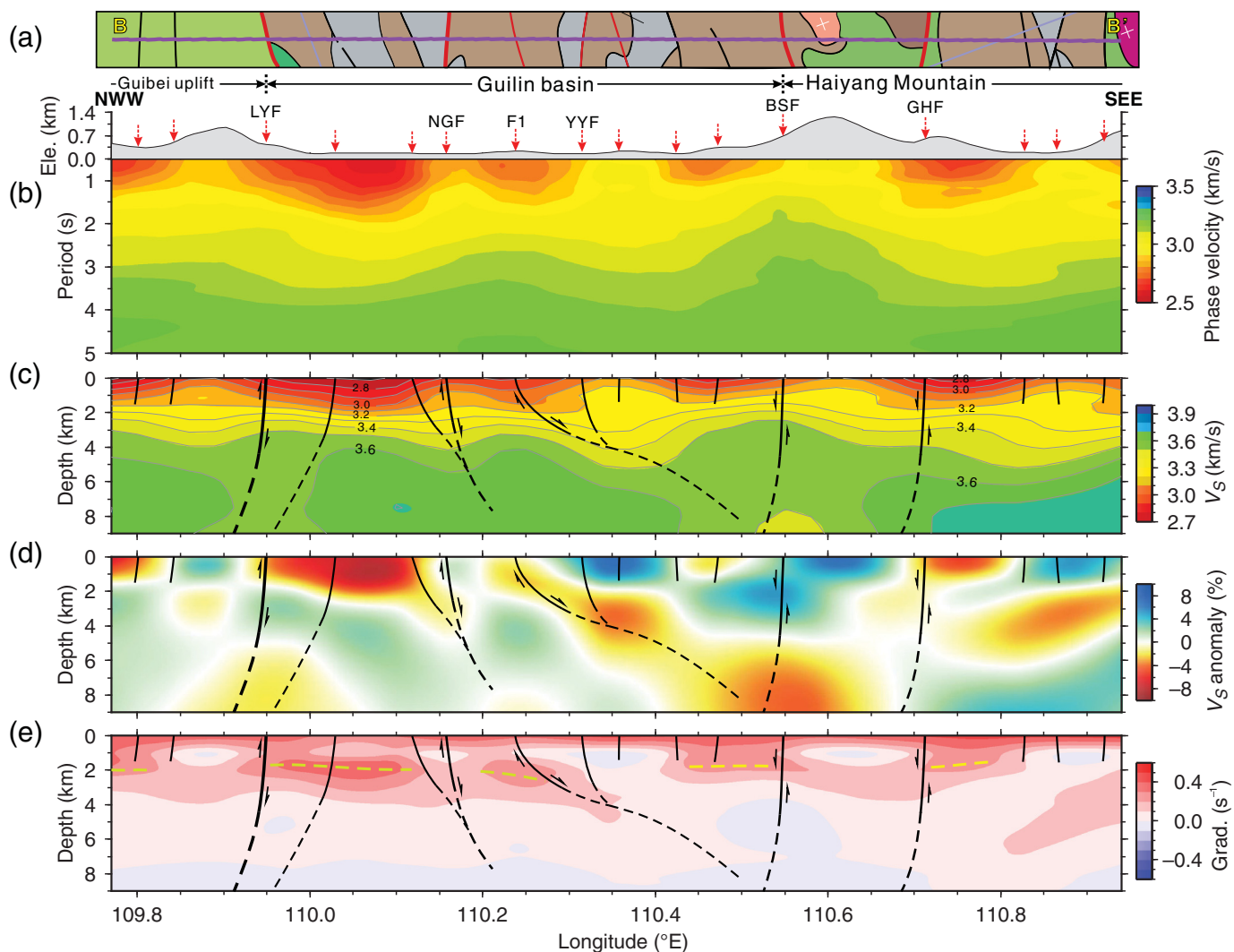
Because the V_S structure is obtained by inverting the local path dispersion curve below each grid point, the lateral resolution for V_S inversion is equivalent to that of the previous phase velocity inversion. The relative V_S anomaly image (Fig. 7d) shows that the minimum horizontal scales of stable anomalies range generally between 0.10° and 0.25° from top to bottom. Therefore, the resolution of the inversion results obtained here is basically that found for the main velocity anomalies.

With the purpose of analyzing the influence of the initial velocity model on the inversion results, we take into account five different initial velocity models (Fig. 10a), namely: model M1 used in this article, homogeneous model M2, linear model M3, model M4 with low velocity at depth, and model M5 with high- V_P/V_S ratio compared to other models. The V_P/V_S ratio is 1.70 for the M1-M4 models and 1.76 for the M5 model; the V_S structure of M5 is the same as that of M1. As an example, we take the local path dispersion relative to the grid point (110.50° E, 25.09° N) and use the same parameters for inversion. In Figure 10b we can see the inversion results, that is, the

Figure 6. (a-i) S-wave velocity horizontal slices at different depths from 1 to 9 km (upper left corner) and corresponding average S-wave velocities for each period are 2.95, 3.20, 3.39, 3.44, 3.46, 3.50, 3.53, 3.55, and 3.57 km/s. The velocity scale can be seen in the upper right corner of each graph. The circles in (a) indicate the positions of the four grid points in Figure 5.

best-fitting shear-wave velocity models obtained from the previously described initial models and the dispersion curve taken as reference. These results indicate that the inversion error above 12 km depth is less than 3.0% for all trial models, and that the error within the upper 1–6 km is less than 1.5%. In fact, the variations in V_S related to the main anomalies are generally greater than 2% (Fig. 7d). Therefore, the selection of the initial velocity model basically does not affect the inversion and identification of main velocity anomalies. Figure 10c shows the good coincidence between the reference local dispersion curve and the synthetic dispersion curves calculated from the inverted models M1–M5.

The vertical resolution of surface wave is generally low and is positively related to frequency. Figure S3 shows the Rayleigh-wave phase velocity sensitive kernel functions for the best-



fitting velocity model and periods from 1.0 to 5.0 s. The longest period of phase velocity used in this article is 5 s. Its kernel function shows that this period is sensitive to the crustal structure at depths of ~ 6 km, with resolution gradually decreasing below 6 km with increasing depth. Considering the resolving kernels (Fig. S3) and the previously mentioned uncertainties affecting V_S (Fig. 10b), we can only explain the continuous and well-scaled velocity anomalies above ~ 6 km depth, but not the small local anomalies at greater depths and neither the anomalies at the edge of the survey area.

Discussion

Tectonic evolution of the Guilin basin

Geological data show that the Guilin Karst basin was formed as early as the Cretaceous, and that its crystalline basement is composed of a Caledonian fold belt of pre-Devonian clastic rocks. From the Cambrian to the Middle Triassic, the Guilin area was in depression or subsidence for a long time. Carbonate rocks deposited in the Devonian and Carboniferous of the Late Paleozoic are the main sedimentary layers in this area (Chen and Liu, 1980; Wang *et al.*, 2013). Both the Indosinian and

Figure 7. (a) Reference profile BB' (purple straight line) crossing the Guilin basin (and other geological formations) from north-west to southeast (see the purple line in the middle of Fig. 1a for the position of the profile). (b) Vertical section showing the period-dependent phase velocity structure along the reference profile. The topographic relief has been included (top) and also the main faults intersected by the profile (marked with their respective acronyms). (c) Shear-wave velocity (V_S) structure. (d) Relative V_S anomaly (in percentage). (e) Vertical V_S gradient. Black dashed lines in plots (c–e) depict inferred faults (arrows indicate direction of fault movement). The yellow dashed line in plot (e) denotes a high-velocity discontinuity.

Yanshanian movements had a severe impact on this area, but there are no Tertiary sediments in the basin, indicating that it has been slowly rising and subjected to weathering and denudation since the Himalayan movement cycle (from Late Cretaceous to present, BGGX, 1976). Our V_S results show that the main tectonic trend of the Guilin basin is almost north-south. The northern and southern sides of the basin are mainly controlled by northwest- and northeast-trending faults, whereas

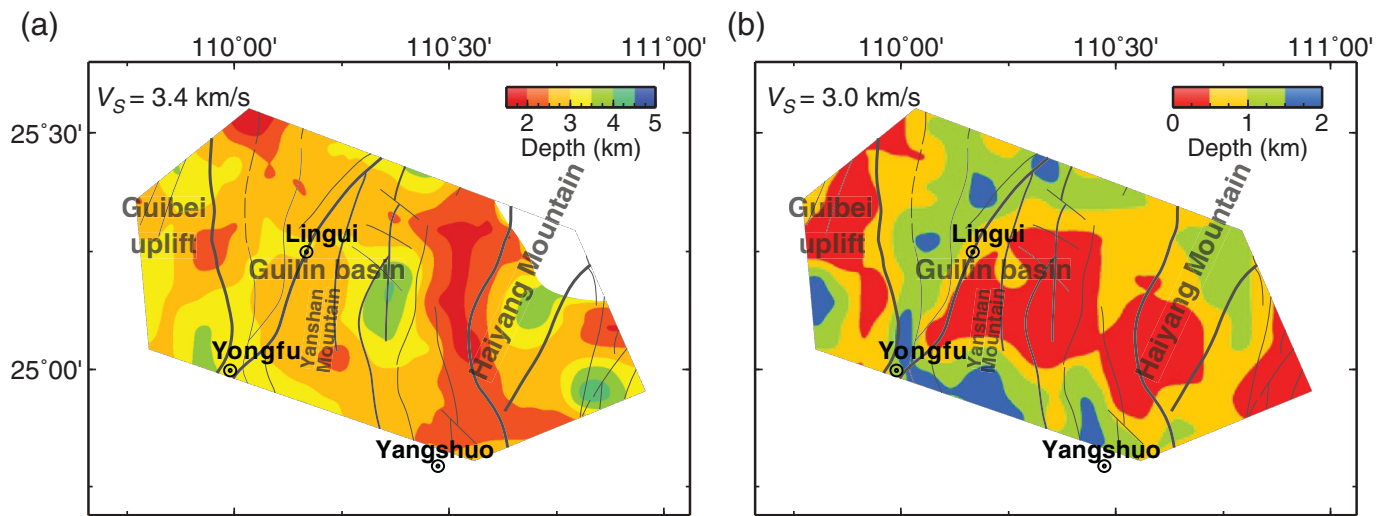


Figure 8. Surfaces of equal V_S velocity of (a) 3.4 and (b) 3.0 km/s. Reference velocity is indicated in the upper left corner and depth

scale is included in the upper right corner of each graph.

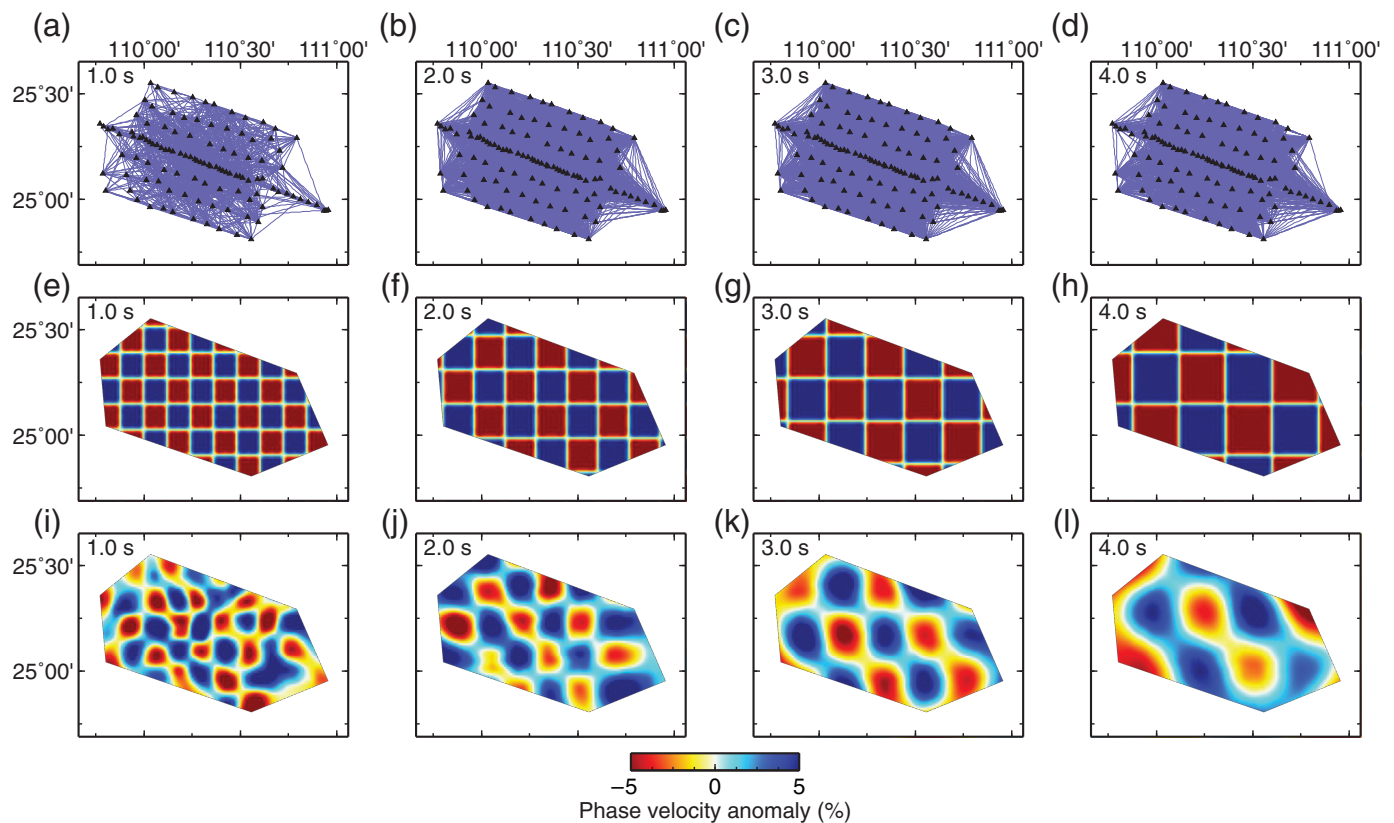
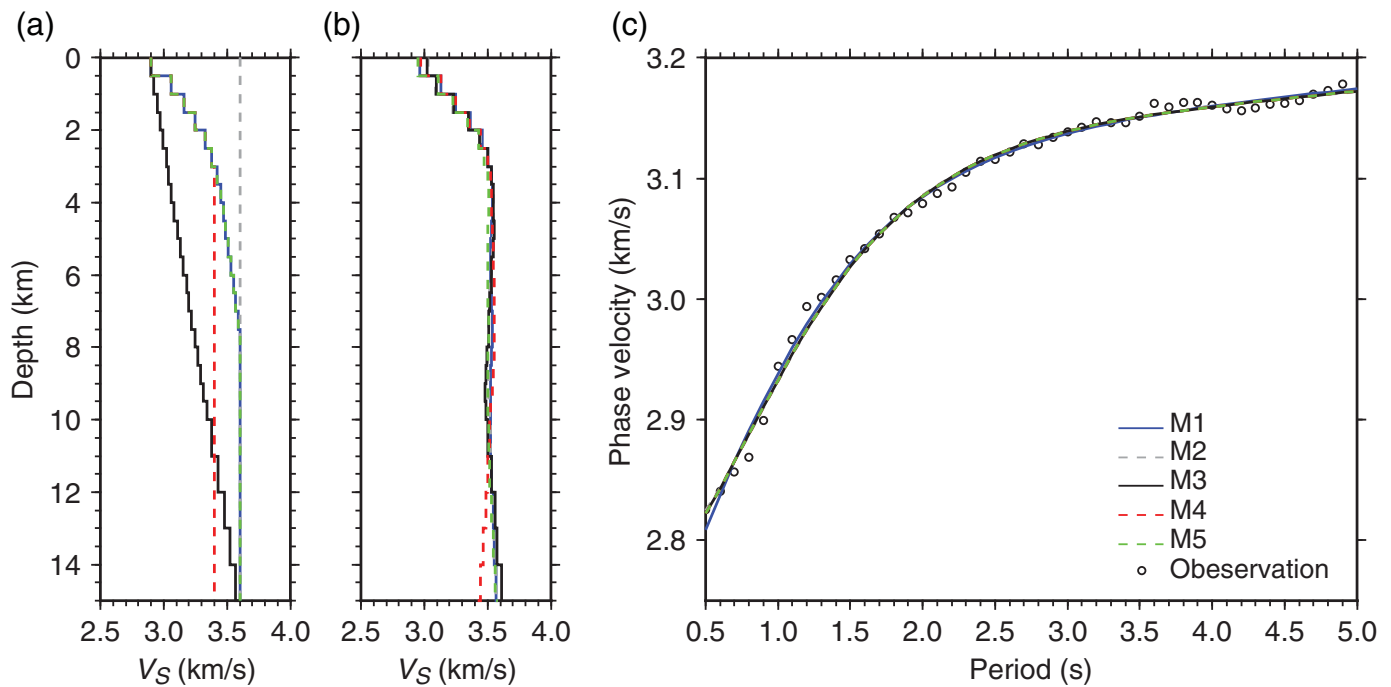


Figure 9. Checkerboard test for phase velocity inversion. (a–d) Ray-path coverage for periods from 1.0 to 4.0 s. Black triangles indicate the stations, and blue straight lines are ray

paths. (e–h) Trial checkerboards with increasing grid sizes, 0.12°, 0.16°, 0.20°, and 0.24°, depending on the period. (i–l) Corresponding output lattice models.



the western and eastern sides are controlled by the Longsheng–Yongfu and Baishi faults, respectively. Faults generally developed in the basin showing a fault block structure with an uneven distribution of sediment thickness. The V_S images at different depths (Figs. 6, 8) reflect the change of sedimentary morphology in the basin. The average thickness of the sediment is 1–3 km, although locally it can reach 3–4 km. The famous Guilin–Yangshuo area has a thick sedimentary layer, and the evolution of this local karst basin is controlled by the Yaoshan–Yanshan and Baishi faults.

Our imaging results show that the Longsheng–Yongfu, Nanning–Guilin, Baishi, and Guanyang–Hengyang faults are all large basement faults. Among them, the Longsheng–Yongfu and Baishi faults are important regional tectonic boundaries, which separate three tectonic units (Fig. 1): Guibei uplift, Guilin basin (or Guilin arc fold-fault belt), and Haiyang Mountain (or Haiyangshan fold-fault belt). Our results reveal that the Longsheng–Yongfu fault with nearly north–south strike tends to west with a large dip angle, and that the geological structures on both sides of the fault are significantly different. According to the geological data, the Guibei uplift to the west of the fault began to rise during the Sibao movement. After multistage tectonic evolution, large geological differences gradually emerged on both sides of the fault. As for the Baishi fault to the east of Guilin, its general strike shows an arc shape that protrudes to the west. From the multiattribute images (Fig. 7), it can be seen that the fault is trending west with obvious velocity differences on both the sides, controlling the sedimentary morphology of the Guilin basin in the west.

The Nanning–Guilin fault in the Guilin area can be divided into two northeast and southwest sections, and it is locally hidden. Geological data indicate that this fault is northeast-

Figure 10. Comparison of inversion results obtained from different initial velocity models. The local path dispersion curve at the grid point (110.50° E, 25.09° N) is taken as reference. (a) Five different initial models (labeled M1–M5). (b) Best-fitting shear-wave velocity models obtained by inversion of dispersion data. (c) Reference dispersion curve (small circles) and synthetic dispersion curves (continuous and dashed lines) calculated from the inverted models M1–M5.

trending and was formed during the Mesozoic Yanshanian movement (BGMRGX, 1985). Our V_S results further clarify the trend of its southwest section. Different from the steep-dipping Longsheng–Yongfu and Baishi faults, we find that the Nanning–Guilin fault in the south of Lingui District is characterized by gentle dip. In addition, it is interesting that the Nanning–Guilin and Yaoshan–Yanshan faults and the F1 fault between them (Fig. 7; Figs. S1, S2) all tend to the southeast. There are amplitude differences among their corresponding low-velocity anomalies in the AA', BB', and CC' sections, but the overall characteristics are similar. We speculate that they are all branches of the Nanning–Guilin fault, that is, the Nanning–Guilin fault is a fault zone composed of several roughly parallel subfaults, and it may also play a certain role in the formation and evolution of the Guilin Karst basin (Nie *et al.*, 2019).

Implications for urban planning and disaster mitigation

As mentioned earlier, Guilin city not only faces common geological disasters affecting modern urban construction, such as tectonic earthquakes, but also faces some special geological disasters in karst areas, such as soil and water losses, karst

collapses, and tectonic-subsidence earthquakes. These problems can be addressed through the detection and analysis of the high-resolution structure of the urban underground space.

The karst landform in the Guilin area causes serious soil erosion and lack of surface water resources. However, the previous geological investigations show that the groundwater level in Guilin area generally fluctuates near the bedrock (limestone) surface, which causes the karst landform to be very developed in the whole area, accompanied by abundant karst groundwater (Li and Nie, 2020). The statistical results further reveal that the distribution of karst in Guilin area is basically consistent with the distribution of thick Devonian sedimentary strata (Long *et al.*, 2015; Li and Nie, 2020), so it can be concluded that the sediment thickness is positively related to the development of karst and groundwater. Accordingly, we speculate that the groundwater resources in valleys or sub-basins (such as the Li river valley between Yanshan Mountain and Haiyang Mountain, and the Yi river valley in Yongfu County) with thick sedimentary layers and surface runoff recharge may be especially rich and can be used as important options for urban water supply. In addition, the tracer test results of hydrochemistry show that the runoff of karst groundwater in Guilin area is very large, sometimes even exceeding the surface runoff, and the direction of karst groundwater channels is mainly controlled by a series of north-south folds and faults (Liu *et al.*, 2015; Jiang *et al.*, 2019). In fact, it is easy to understand the control of fault strike on the direction of groundwater runoff. Compared with complete limestone, there is no doubt that the fault fracture zone is more conducive to the erosion and circulation of groundwater. Certainly, areas with thick sedimentary layers also face the problem of frequent geological disasters such as karst collapse (Qian, 2007). Therefore, it is also necessary to carry out an accurate detection of possible underground karst caves by way of collapse prevention.

The earthquake risk level in the Guilin area is generally low, but small-scale tectonic earthquakes can easily cause karst collapse. The conjunction of these two disasters is known as tectonic-subsidence earthquake (Miu, 1998; Yu and Gao, 2017; Chen and Tang, 2018). The historical earthquake records show that the earthquakes in Guilin area are generally dominated by low-magnitude and high-intensity tectonic-subsidence earthquakes (Miu, 1998; Long *et al.*, 2015; Yu and Gao, 2017; Chen and Tang, 2018; Li and Nie, 2020), which mainly occurred in bare and covered karst areas. In the area where karst is particularly developed, even a small earthquake can bring great loss of life and property to human beings. For example, the 1997 M_w 1.2 tectonic-subsidence earthquake in Yanshan District resulted in the collapse of four houses, serious cracking or subsidence of 28 houses, and slight cracking of several houses (Long *et al.*, 2015); the small tectonic-subsidence earthquake in 2012 (without complete records) in the urban area of Guilin city caused direct economic losses of more than 4 million Renminbi (Li and Nie, 2020). Therefore, it is necessary for us to evaluate which regions

are high-risk regions of tectonic-subsidence earthquakes and to further take some preventive measures.

We know that tectonic earthquake and karst landform are two key conditions required for the occurrence of tectonic-subsidence earthquake (Miu, 1998). First of all, both the geological data and historical earthquake records show that the Nanning-Guilin, Longsheng-Yongfu, and Yaoshan-Yanshan are the three main active faults, the first of them being the most active. The most of the historical tectonic-subsidence earthquakes are distributed along the Nanning-Guilin fault (Miu, 1998; Long *et al.*, 2015; Yu and Gao, 2017; Chen and Tang, 2018; Li and Nie, 2020), including the 1599 M_w 5 Lingchuan earthquake and the 1917 M_w 3 Quanzhou earthquake. Therefore, we need to pay more attention to the karst development along this fault. However, the constraint scope of surface geological survey on karst is very limited (Long *et al.*, 2015; Jiang *et al.*, 2019; Li and Nie, 2020). Fortunately, the ambient noise tomography in this article can provide detailed deep structure constraints. Our imaging results show that the sedimentary layer along the Nanning-Guilin fault is relatively thick, and the rocks along the fault zone are broken (with low- V_S anomaly). Under the condition that the groundwater level in Guilin area is generally shallow, this fault zone is fully equipped with conditions for karst development. Therefore, the risk of small- and medium-sized tectonic and tectonic-subsidence earthquakes along the Nanning-Guilin fault is relatively high. In addition, the thick low-velocity sedimentary layers along the fault zone have an amplification effect on seismic signals, which can further aggravate the potential destructive effect of an earthquake (Luo *et al.*, 2011; Hong *et al.*, 2017). The Nanning-Guilin fault just obliquely crosses the new urban area of Guilin city (Lingui District), and the sedimentary layer along the fault is thick. Therefore, we suggest that those standards that can improve the earthquake-resistant behavior of buildings be taken into account in the construction of this new urban area.

Conclusions

Using a dense short-period seismic array together with ambient noise surface-wave tomography, we have been able to investigate the high-resolution V_S structure above the first 9 km depth below the Guilin city area. We have reached the following conclusions:

1. Longsheng-Yongfu, Nanning-Guilin, Yaoshan-Yanshan, Baishi, and Guanyang-Hengyang faults may be large basement faults. Among them, the Nanning-Guilin fault is a fault zone composed of several roughly parallel subfaults. The formation and evolution of the Guilin faulted basin are mainly controlled by the steep-dipping Longsheng-Yongfu and Baishi faults, and it is partially controlled by the gently dipping Nanning-Guilin fault in the interior of the basin.
2. Sedimentary layers are relatively thick between Yanshan Mountain and Haiyang Mountain and along the Yi river

valley to the north of Yongfu County, where karst groundwater may be abundant and used as an important option for urban water supply. The risk of small- and medium-sized tectonic and tectonic-subsidence earthquakes along the partially buried Nanning–Guilin fault is relatively high. The V_s tomography results presented in this study can play an important role in urban planning and hazard mitigation associated with these buried faults.

Data and Resources

The data collected in this project are currently managed by Zhi Zhang, and any collaborative work with this dataset is welcome. For those people interested in the dataset, send an e-mail to Zhi Zhang (zhangzhi@glut.edu.cn). The specific coordinates and elevation of each station, as well as the multiattribute images (results) related to profiles AA' and CC' (Fig. 1a), are included in the supplemental material.

Declaration of Competing Interests

The authors acknowledge that there are no conflicts of interest recorded.

Acknowledgments

The authors would like to thank three anonymous reviewers whose helpful comments and observations have allowed us to substantially improve the presentation of this article. This work was supported by the National Natural Science Foundation of China (Grant Numbers 41974048, 42104042, and 42104040), the Guangxi Natural Science Foundation (Grant Numbers 2018GXNSFAA138059 and 2018GXNSFBA050005), the China Postdoctoral Science Foundation (Grant Number 2020M683627XB), the Guangxi Science and Technology Base and Talent Project (Guike AD19110057), and the Guangxi Collaborative Innovation Center for the Exploration of Hidden Non-ferrous Metal Deposits and the New Materials Development Project.

References

Adly, A., V. Poggi, D. Fäh, A. Hassoup, and A. Omran (2017). Combining active and passive seismic methods for the characterization of urban sites in Cairo, Egypt, *Geophys. J. Int.* **210**, 428–442.

Artemieva, I. M., and H. Thybo (2013). EUNaseis: A seismic model for Moho and crustal structure in Europe, Greenland, and the North Atlantic region, *Tectonophysics* **609**, 97–153.

Badal, J., Y. Chen, M. Chourak, and J. Stankiewicz (2013). S-wave velocity images of the Dead Sea Basin provided by ambient seismic noise, *J. Asian Earth Sci.* **75**, 26–35.

Bensen, G. D., M. H. Ritzwoller, M. P. Barmin, A. L. Levshin, F. Lin, M. P. Moschetti, N. M. Shapiro, and Y. Yang (2007). Processing seismic ambient noise data to obtain reliable broad-band surface wave dispersion measurements, *Geophys. J. Int.* **169**, no. 3, 1239–1260, doi: [10.1111/j.1365-246X.2007.03374.x](https://doi.org/10.1111/j.1365-246X.2007.03374.x).

Bureau of Geology of Guangxi Province (BGGX) (1976). 1:50000 regional geological survey report of Guilin, 543 Factory Press.

Bureau of Geology and Mineral Resources of Guangxi Province (BGMRGX) (1985). *The Regional Geology Annals of Guangxi Province*, Geological Publishing House, Beijing, China, 853 pp. (in Chinese).

Campillo, M., and P. Roux (2015). Crust and lithospheric structure—Seismic imaging and monitoring with ambient noise correlations, in *Treatise on Geophysics*, G. Schubert (Editor), Second Ed., Vol. 1, Elsevier, Oxford, United Kingdom, 391–417.

Chen, W., and G. L. Tang (2018). A study on the tourism resources of Karst World Natural Heritage site in Guilin, *J. Guilin Norm. Coll.* **32**, no. 4, 43–47.

Chen, X. H., H. Y. Zhang, C. J. Zhou, J. Y. Pan, H. X. Xing, and X. J. Chang (2021). Using ambient noise tomography and MAPS for high resolution stratigraphic identification in Hangzhou urban area, *J. Appl. Geophys.* **189**, 104327, doi: [10.1016/j.jappgeo.2021.104327](https://doi.org/10.1016/j.jappgeo.2021.104327).

Chen, Z. P., and J. R. Liu (1980). The discussion of the evolution history for Guilin basin, *Acta Geogr. Sin.* **35**, no. 4, 338–347.

Cheng, F., J. H. Xia, Y. X. Xu, Z. B. Xu, and Y. D. Pan (2015). A new passive seismic method based on seismic interferometry and multi-channel analysis of surface waves, *J. Appl. Geophys.* **117**, 126–135.

Diaz, J., M. Ruiz, P. S. S. Pastor, and P. Romero (2017). Urban seismology: On the origin of earth vibrations within a city, *Sci. Rep.* **7**, 1–11, doi: [10.1038/s41598-017-15499-y](https://doi.org/10.1038/s41598-017-15499-y).

Diaz, J., M. Schimmel, M. Ruiz, and R. Carbonell (2020). Seismometers within cities: A tool to connect Earth sciences and society, *Front. Earth Sci.* **8**, 9, doi: [10.3389/feart.2020.00009](https://doi.org/10.3389/feart.2020.00009).

Fang, G., Y. E. Li, Y. M. Zhao, and E. R. Martin (2019). Urban near-surface seismic monitoring using distributed acoustic sensing, *Geophys. Res. Lett.* **47**, e2019GL086115, doi: [10.1029/2019GL086115](https://doi.org/10.1029/2019GL086115).

Fang, H. J., H. J. Yao, H. J. Zhang, Y. C. Huang, and R. D. van der Hilst (2015). Direct inversion of surface wave dispersion for three-dimensional shallow crustal structure based on ray tracing: Methodology and application, *Geophys. J. Int.* **201**, no. 3, 1251–1263, doi: [10.1093/gji/ggv080](https://doi.org/10.1093/gji/ggv080).

Feng, Z. H., X. F. Li, M. H. Zhang, and J. C. Liang (2001). Distribution of karst collapses and its relation to geological structures in the Guilin urban and suburban areas, Guangxi province, *J. Geol. Hazards Environ. Preserv.* **12**, no. 2, 16–20.

Goertz, A., B. Schechinger, B. Witten, M. Koerbe, and P. Krajewski (2012). Extracting subsurface information from ambient seismic noise—A case study from Germany, *Geophysics* **77**, no. 4, KS13–KS31.

Herrmann, R. B. (2013). Computer programs in seismology: An evolving tool for instruction and research, *Seismol. Res. Lett.* **84**, no. 6, 1081–1088, doi: [10.1785/0220110096](https://doi.org/10.1785/0220110096).

Herrmann, R. B., and C. J. Ammon (2013). Surface wave, receiver functions and crustal structure, in *Computer Programs in Seismology*, Saint Louis University, available at <http://www.eas.slu.edu/People/RBHerrmann/ComputerPrograms.html> (last accessed December 2013).

Hong, D. Q., P. Zhao, H. Y. Ni, B. Zhang, and X. L. Wang (2017). Determination of seismic source depth of Fuyang M_s 4.3 earthquake and analysis of seismogenesis, *Chinese J. Geophys.* **60**, no. 4, 1423–1432.

Huang, Q. B., X. Q. Qin, P. P. Tang, and P. Y. Liu (2013). The characteristic and significance of carbon isotope ($\delta^{13}C_{DIC}$) and oxygen isotope ($\delta^{18}O$) value in different type of karst water in Guilin, *Geochimica* **42**, no. 1, 64–72.

Jiang, G. H., F. Guo, and C. Y. Tang (2019). Groundwater systems in bare and covered karst aquifers: Evidence from tracer tests, hydrochemistry, and groundwater ages, *Environ. Earthq. Sci.* **78**, 608.

- Jiang, S. Y., F. Wu, Q. C. Liu, Y. He, and H. L. Li (2020). Karst development characteristics and distribution in Guilin urban planning center of Guangxi Zhuang Autonomas Region, *Chin. J. Geol. Hazard Control* **30**, no. 3, 120–128.
- Li, C., H. J. Yao, H. J. Fang, X. L. Huang, K. S. Wan, H. J. Zhang, and K. D. Wang (2016). 3D near-surface shear-wave velocity structure from ambient-noise tomography and borehole data in the Hefei urban area, China, *Seismol. Res. Lett.* **87**, 882–892.
- Li, D. Q., Y. C. Zhang, R. H. Xue, B. P. Du, X. Y. Li, Y. X. Li, and K. F. Shi (2010). Application of CSAMT to detection of active faults, *Prog. Geophys.* **25**, no. 4, 1387–1395.
- Li, L., and G. J. Nie (2020). Types and distribution characteristics of secondary geological disasters in Guangxi, *J. Catastrophol.* **35**, no. 3, 118–124.
- Li, L. L., X. L. Huang, H. J. Yao, P. Miao, X. L. Wang, Z. W. Bao, H. Y. Ni, C. Li, Y. Yang, S. Luo, *et al.* (2020). Shallow shear wave velocity structure from ambient noise tomography in Hefei city and its implication for urban sedimentary environment, *Chin. J. Geophys.* **63**, no. 9, 3307–3323.
- Li, X. J. (2011). Applications and development of city geophysical prospecting in China, *Prog. Geophys.* **26**, no. 6, 2221–2231.
- Liang, F., L. Gao, Z. H. Wang, H. L. Li, K. Liu, T. Wang, and X. Z. Li (2019). Study of the shear wave velocity structure of underground shallow layer of Jinan by ambient noise tomography, *Earth Sci. Front.* **26**, no. 3, 129–139.
- Liang, F. Y., and B. Xu (2014). Discrimination of tower-, cockpit-, and non-karst landforms in Guilin, Southern China, based on morphometric characteristics, *Geomorphology* **204**, 42–48.
- Liu, S. H., F. Guo, G. H. Jiang, Q. J. Tang, X. J. Guo, and S. Y. Huang (2015). Hydrogeochemical characteristics of peak forest plain in Guilin city, China, *Earth Environ.* **43**, no. 3, 55–65.
- Liu, Y., H. J. Zhang, H. J. Fang, H. J. Yao, and J. Gao (2018). Ambient noise tomography of three-dimensional near-surface shear-wave velocity structure around the hydraulic fracturing site using surface microseismic monitoring array, *J. Appl. Geophys.* **159**, 209–217.
- Long, A. M., J. B. Wu, C. H. Yan, and S. Y. Deng (2015). Collapse earthquake research and disaster prevention and mitigation measures in Guangxi, South China, *J. Seismol.* **35**, no. 4, 1–9.
- Lu, Y. R., K. H. Zhou, X. Bai, Q. Tian, X. T. Tang, and Z. Z. Wei (2019). Causes and manifestations of sedimentary facies differentiation of Carboniferous strata in northern Guangxi, *Land Resour. South. China* **8**, 50–53.
- Luo, Y., S. D. Ni, X. F. Zeng, J. Xie, R. Chen, and F. Long (2011). The M 5.0 Suining-Tongnan (China) earthquake of 31 January 2010: A destructive earthquake occurring in sedimentary cover, *Chinese Sci. Bull.* **56**, 521–525, doi: [10.1007/s11434-010-4276-z](https://doi.org/10.1007/s11434-010-4276-z).
- Luo, Y. H., Y. J. Yang, Y. X. Xu, H. R. Xu, K. F. Zhao, and K. Wang (2015). On the limitations if interstation distances in ambient noise tomography, *Geophys. J. Int.* **201**, 652–661.
- Ma, L. F., X. F. Qiao, L. R. Min, B. X. Fan, X. Z. Ding, W. L. Xu, X. Liu, D. S. Yao, D. Q. Zhang, P. T. Gu, *et al.* (2004). *Geological Atlas of China*, Institute of Geology, Chinese Academy of Geological Sciences, Beijing, China.
- Miu, Z. L. (1998). The distribution and occurrence of karst collapse-induced earthquakes in Guilin, *Hydrogeol. Eng. Geol.* **4**, 38–41.
- Montagner, J. P., and H. C. Nataf (1986). A simple method for inverting the azimuthal anisotropy of surface waves, *J. Geophys. Res.* **91**, no. B1, 511–520.
- Nafe, J. E., and C. L. Drake (1957). Variation with depth in shallow and deep water marine sediments of porosity, density and the velocities of compressional and shear waves, *Geophysics* **22**, no. 3, 523–552.
- Nie, G. J., S. He, H. Li, and J. H. Lu (2019). The Cenozoic activity characteristics and tectonic setting of the faults in Guangxi, *North China Earthq. Sci.* **37**, 7–11.
- Nolet, G. (2008). *A Breviary of Seismic Tomography*, Cambridge University Press, Cambridge, United Kingdom.
- Picozzi, M., S. Parolai, D. Bindi, and A. Strollo (2009). Characterization of shallow geology by high-frequency seismic noise tomography, *Geophys. J. Int.* **176**, 164–174.
- Qian, J. P. (2007). Basic characteristics of karstic collapse in Guilin city and its prevention countermeasures, *Miner. Resour. Geol.* **21**, no. 2, 200–204.
- Sabra, K. G., P. Gerstoft, P. Roux, and W. A. Kuperman (2005). Extracting time-domain Green's function estimates from ambient seismic noise, *Geophys. Res. Lett.* **32**, no. 3, L03310, doi: [10.1029/2004GL021862](https://doi.org/10.1029/2004GL021862).
- Schwab, F. A., and L. Knopoff (1972). Fast surface wave and free mode computations—ScienceDirect, in *Methods in Computational Physics: Advances in Research and Applications*, B. A. Bolt (Editor), Vol. 11, Elsevier, Oxford, United Kingdom, 87–180.
- Shapiro, N. M., and M. Campillo (2004). Emergence of broadband Rayleigh waves from correlations of the ambient seismic noise, *Geophys. Res. Lett.* **31**, no. 7, 1–4, doi: [10.1029/2004gl019491](https://doi.org/10.1029/2004gl019491).
- Shapiro, N. M., M. Campillo, L. Stehly, and M. H. Ritzwoller (2005). High-resolution surface-wave tomography from ambient seismic noise, *Science* **307**, no. 5715, 1615–1618, doi: [10.1126/science.1108339](https://doi.org/10.1126/science.1108339).
- Shearer, P. M. (2009). *Introduction to Seismology*, Second Ed., Cambridge University Press, Cambridge, United Kingdom.
- Tang, T., and M. J. Day (2000). Field survey and analysis of hillslopes on tower karst in Guilin, southern China, *Earth Surf. Process. Landf.* **25**, 1221–1235.
- Tarantola, A., and B. Valette (1982). Generalized nonlinear inverse problems solved using the least squares criterion, *Rev. Geophys.* **20**, no. 2, 219–232.
- Thybo, H., T. Janik, V. D. Omelchenko, M. Grad, R. G. Garetsky, A. A. Belinsky, G. I. Karatayev, G. Zlotski, M. E. Knudsen, R. Sand, *et al.* (2003). Upper lithospheric seismic velocity structure across the Pripyat Trough and the Ukrainian Shield along the EUROBRIDGE'97 profile, *Tectonophysics* **371**, 41–79.
- Vassallo, M., R. D. Matteis, A. Bobbio, G. D. Giulio, G. M. Adinolfi, L. Cantore, R. Coglianò, A. Fodarella, R. Maresca, S. Pucillo, *et al.* (2019). Seismic noise cross-correlation in the urban area of Benevento city (Southern Italy), *Geophys. J. Int.* **217**, 1524–1542.
- Wan, Z. Q., S. Q. Qin, and S. W. Qi (2001). The karstic collapse and its protection in Guilin city, *J. Eng. Geol.* **9**, no. 2, 199–203.
- Wang, C. S., C. H. Zhou, J. B. Peng, J. Fan, H. H. Zhu, X. Z. Li, G. H. Cheng, C. S. Dai, and N. X. Xu (2019). A discussion on high-quality development and sustainable utilization of China's urban underground space in the new era, *Earth Sci. Front.* **26**, no. 3, 1.

- Wang, P. M., J. H. Yu, T. Sun, Y. Shi, P. R. Chen, K. D. Zhao, W. F. Chen, and Q. Liu (2013). Composition variations of the Sinian-Cambrian sedimentary rocks in Hunan and Guangxi provinces and their tectonic significance, *Sci. China* **56**, no. 11, 1899–1917.
- Weaver, R. L. (2005). Information from seismic noise, *Science* **307**, no. 5715, 1568–1569, doi: [10.1126/science.1109834](https://doi.org/10.1126/science.1109834).
- Wei, W. S., and W. X. Zhou (2000). Preliminary study on factors controlling buried geothermal in Guilin, *Carsologica Sin.* **19**, no. 2, 152–158+163.
- Yang, Y. J., M. H. Ritzwoller, A. L. Levshin, and N. M. Shapiro (2007). Ambient noise Rayleigh wave tomography across Europe, *Geophys. J. Int.* **168**, no. 1, 259–274, doi: [10.1111/j.1365-246X.2006.03203.x](https://doi.org/10.1111/j.1365-246X.2006.03203.x).
- Yao, H. J., R. D. van der Hilst, and M. V. de Hoop (2006). Surface-wave array tomography in SE Tibet from ambient seismic noise and two-station analysis—I. Phase velocity maps, *Geophys. J. Int.* **166**, no. 2, 732–744, doi: [10.1111/j.1365-246X.2006.03028.x](https://doi.org/10.1111/j.1365-246X.2006.03028.x).
- Yao, H. J., R. D. van der Hilst, and J. P. Montagner (2010). Heterogeneity and anisotropy of the lithosphere of SE Tibet from surface wave array tomography, *J. Geophys. Res.* **115**, no. 24, doi: [10.1029/2009jb007142](https://doi.org/10.1029/2009jb007142).
- Yi, B., Z. F. Zeng, J. Xue, and E. Z. Li (2008). Application of geophysical method in city active fault detection, *Prog. Geophys.* **23**, no. 2, 599–604.
- Yu, D. G., and W. Z. Gao (2017). Karst sinkhole occurrences in Lingui new district of Guilin city, *Soil Eng. Found.* **31**, no. 6, 716–720.
- Yu, G. P., T. Xu, J. T. Liu, and Y. S. Ai (2020). Late Mesozoic extensional structures and gold mineralization in Jiaodong Peninsula, eastern North China Craton: An inspiration from ambient noise tomography on data from a dense seismic array, *Chin. J. Geophys.* **63**, no. 5, 1878–1893.
- Yuan, D. X. (1997). Sensitivity of karst process to environmental change along the PEP II transect, *Quaternary Int.* **37**, 105–113.
- Zeng, Q., R. S. Chu, M. H. Sheng, and Z. G. Wei (2020). Seismic ambient noise tomography for shallow velocity structures beneath Weiyuan, Sichuan, *Chin. J. Geophys.* **63**, no. 3, 944–955.
- Zhang, L. F., X. S. Zeng, Y. S. Yao, and W. L. Liao (2007). Review on karst collapse in China, *Chin. J. Geol. Hazard Control* **18**, no. 3, 126–130.
- Zhang, M. H., J. Y. Liang, C. P. Ouyang, W. L. Wei, and Z. L. Miao (2001). The relation between geological structure and heat-generating in western area of Guilin, *J. Guilin Inst. Technol.* **21**, no. 3, 213–217.
- Zhang, M. H., Y. S. Liu, J. Hou, T. Xu, and Z. M. Bai (2019). Review of seismic tomography methods in near-surface structures reconstruction, *Prog. Geophys.* **34**, no. 1, 48–63.
- Zhang, W. K., X. P. Xu, and C. Li (2019). The application of CSAMT and MT in searching for urban geothermal resources, *J. Qinghai Univ.* **37**, no. 4, 77–82.
- Zhao, P., J. Jiang, and X. R. Wang (2017). Urban underground space exploration key technologies and development trend, *Coal Geol. China* **29**, no. 9, 61–66.
- Zheng, L. M., X. P. Fan, P. Zhang, J. R. Hao, H. Qian, and T. Zheng (2021). Detection of urban hidden faults using group-velocity ambient noise tomography beneath Zhenjiang area, China, *Sci. Rep.* **11**, 987.
- Zheng, M., Z. M. Bai, T. Xu, and J. Badal (2021). Upper crustal velocity structure of the Ailaoshan-Red River shear zone and its implication for Cenozoic tectonic-magmatic activity: Evidence from ambient noise tomography using short-period dense seismic array, *Phys. Earth Planet. In.* **311**, 106643, doi: [10.1016/j.pepi.2021.106643](https://doi.org/10.1016/j.pepi.2021.106643).
- Zhou, J. C., J. G. Qin, Q. Zhang, C. L. Zhang, and S. Q. Jiang (2015). Vegetation, climate and depositional changes since the middle Holocene in the karst area of Guilin, Guangxi, *Chin. Sci. Bull.* **60**, 1197–1206.

Manuscript received 23 February 2022

Published online 25 October 2022